Journal of Materials Chemistry A

ROYAL SOCIETY OF CHEMISTRY

PAPER

View Article Online
View Journal





Cite this: DOI: 10.1039/d2ta10043f

# Accelerated discovery of cost-effective Nd–Fe–B magnets through adaptive learning†

Jie Chen, [a] Jian Liu,[a] Minjuan Zhang, *[a] Zhanji Dong,[b] Zhongjie Peng,[b] Xinyi Ji,[c] Mei Liu, [c] Lanting Zhang, [c] Anqi Zhang[d] and Hong Zhu [d]

Designing Nd–Fe–B-based permanent magnets with exceptional high temperature stability is a critical step for extending their use in traction motors with an operating temperature of ~150 °C. Conventionally, the high temperature stability is achieved through doping heavy rare-earth elements such as Dy, Tb, *etc.*, which leads to elevated cost in the meantime. Efforts towards doping Nd–Fe–B with lower-cost elements such as La, Ce, and Y, and leveraging the temperature stability with Co and Ni to retain high-temperature performance (remanence and coercivity) have been underway for many years. A critical challenge, however, is the cost in time and resource required for optimizing the doping concentration of these species on a trial-and-error basis. In this work, we demonstrate the utilization of the 'adaptive' learning framework (based on Bayesian Optimization) in the composition optimization of Nd–Fe–B-based magnets: $(Nd_{80}Pr_{20})_{30.80-x-y-z}La_xCe_yY_zFe_{66.67-u-w}Co_uNi_wB_{0.96}M_{1.57}$ (M = Al, Cu, Ga, Ti, in wt%) towards an improved performance–cost ratio. Starting from a limited set of 24 compositions, 9 novel compositions were recommended within 3 iterations, which were then experimentally fabricated, with their magnetic properties measured. The best two candidates identified in the last iteration showed 18.4% and 13.1% improvement in the performance–cost ratio with respect to the benchmark Nd–Fe–B, respectively. The adaptive learning framework proved efficient in screening novel compositions and guiding the experimental design of Nd–Fe–B-based permanent magnets in this work, suggesting great promise for its adoption for other multi-component systems targeting an improved performance–cost ratio.

Received 28th December 2022
Accepted 20th March 2023

DOI: 10.1039/d2ta10043f

rsc.li/materials-a

## 1 Introduction

Nd–Fe–B-based permanent magnets (PMs) are widely used in a range of applications including electric vehicle traction motors, industrial motors, robots, wind turbines as well as various household appliances.[1,2] Despite their excellent room-temperature (RT) magnetic properties, for example, high remanence ($B_r$) and coercivity ($H_{cj}$), these properties of Nd–Fe–B PMs deteriorate rapidly at high temperature (HT). Designing Nd–Fe–B PMs with excellent temperature stability is a critical step for extending their use in applications such as traction motors with operating temperature up to ~150 °C. Conventionally, temperature stability is enhanced through introducing heavy rare-earth (HRE) elements such as Dy, Tb, *etc.*[3–6] The introduction of these HRE elements benefits $H_{cj}$ greatly, especially at HT.[7–12] However, the scarcity and high cost of HRE elements lead to elevated cost, as well as lower $B_r$ in the meantime. Moreover, Nd in itself is a critical element with low reserves and has been subject to high supply risk and ever-growing cost in recent years.[1,13,14] Hence, it is critical to develop competitive and cost-effective Nd–Fe–B PMs with little or no Dy/Tb, as well as reduced usage of Nd.[15–19]

Efforts towards doping (substituting) elements with lower cost, such as La, Ce, and Y to partially replace Nd, and leveraging the temperature stability with Co have been underway for decades.[19–22] La and Ce are more abundant and less costlier than Nd, yet the intrinsic magnetic properties of $La_2Fe_{14}B$/$Ce_2Fe_{14}B$ (for example, saturation magnetization $M_r$, magnetocrystalline anisotropy field $H_a$, and Curie temperature $T_C$) are inferior to those of $Nd_2Fe_{14}B$.[2] As a result, doping of La/Ce invariably leads to degraded magnetic properties, especially at HT.[22–29] Co, with a very high $T_C$, could significantly improve the temperature stability and therefore benefit HT magnetic properties, although it results in loss of RT magnetic properties as well.[21,30–33] In recent years, investigation of Y as a promising doping species for Nd–Fe–B has picked up momentum. Although Y fails to rise above La and Ce in terms of $M_r$ and $H_a$,

[a]Advanced Engineering Research Division, Toyota Motor Technical Research And Service (Shanghai) Co., Ltd, China. E-mail: mindy@ttrssh.com.cn
[b]Yantai Dongxing Magnetic Materials Inc, 888 Yongda Street, Yantai 265500, China
[c]School of Materials Science and Engineering, Shanghai Jiao Tong University, 800 Dongchuan Road, Shanghai 200240, China
[d]University of Michigan–Shanghai Jiao Tong University Joint Institute, Shanghai Jiao Tong University, 800 Dongchuan Road, Shanghai 200240, China

† Electronic supplementary information (ESI) available. See DOI: https://doi.org/10.1039/d2ta10043f

$Y_2Fe_{14}B$ demonstrates a higher $T_C$ than $La_2Fe_{14}B$ or $Ce_2Fe_{14}B$, as well as a positive temperature coefficient of $H_a$ over a wide temperature range, rendering it a promising candidate for enhanced HT magnetic properties.[34–38] In comparison, Ni as a doping species has rarely been reported, as far as we know. A few early studies showed Ni to be favorable for $H_{cj}$ but only at very specific doping ranges, and in general detrimental to $B_r$.[39–41] However, the amount of Ni is generally lower than 1% in these reports, and it is not clear how the doping weight percentage (wt%) beyond 1 wt% would affect magnetic properties, and also importantly, how the temperature stability (and hence HT magnetic properties) is affected by varying amounts of Ni. Given the above findings, we target the doping of the above five species: La, Ce, Y, Co, and Ni, for the composition optimization of Nd–Fe–B PMs in this work, with the goal of achieving excellent magnetic properties at HT (~150 °C). Finding the optimal composition in an efficient manner is highly challenging for a conventional trial-and-error and/or intuition-based approach, due to the vast number of potential combinations in this 5-dimensional composition space. And this is further compounded by the non-linear manner in which the above doping species tend to affect the magnetic properties individually, as well as the complex interaction (for example, reported synergistic effects between La and Ce,[26,30,42] Ce and Y,[35] Ce and Co,[22] *etc.*) among species.

Machine learning (ML) has been widely utilized in a wide range of materials science applications to build predictive models for guiding and accelerating materials design.[43–46] However, robust models capable of making accurate and reliable predictions are usually built upon a large amount of data, which is not always available. In recent years, adaptive-learning framework has shown great promise in the above scenario, where data are scarce and expensive to come by, in terms of both time and cost.[47–51] Fabrication of Nd–Fe–B PMs is one prime example, as it involves many procedures, spanning a duration of months.[4] Large amount of high-quality and consistent samples, therefore, is not usually available for constructing a robust model in one go. The adaptive learning framework tackles this problem by using the following approaches. (1) Kick-start model: constructing a rough initial surrogate model with a very small amount of data. (2) Recommendation: using Bayesian Optimization (BO) to make recommendations for further experimental design to maximize the chance (or gain) of finding the optimal candidate. (3) Update: utilizing experimental feedback to update the surrogate model. The recommendation and update steps are performed iteratively, until the desired target is achieved or the allocated budget is exhausted. At the heart of BO lies the search strategy that leverages the exploration–exploitation trade-off of the corresponding surrogate model, balanced through the maximization of a utility (acquisition) function, which is a measure of the expected gain in target property with respect to current optima.[52] The advantage of this adaptive learning, as compared to conventional ML, is that typically fewer samples are required to build a model of comparable predictive capability.[53] Such methods have been applied in designing new materials,[54–56] as well as materials with enhanced strength,[57–59] tensile strength and electrical conductivity,[60] magnetic properties,[61–64] catalytic performance,[65,66] *etc.*

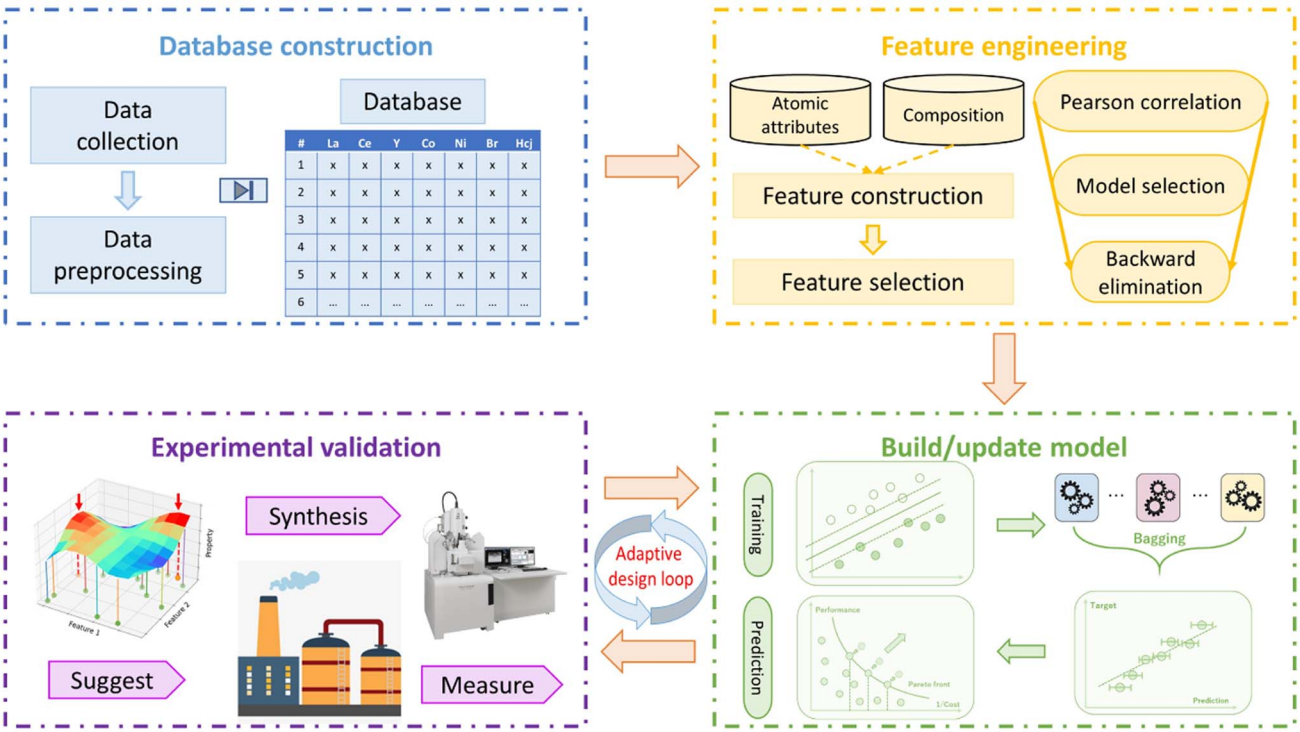


Fig. 1 Flow-chart illustrating the processes of our adaptive-learning framework.

 

Along these lines, we note a recent work by Lambard *et al.*, where the authors utilized BO to directly optimize the extrusion process of hot-deformed Nd–Fe–B, hence achieving a higher energy product.[67] However, cost was not taken into account in their work, and the optimization was for hot-deformed Nd–Fe–B, which is hard to scale-up for industrial mass-production. In this work, we seek to apply the adaptive-learning framework for the composition optimization of sintered Nd–Fe–B PMs, which are widely adopted in industry for scaled-up production. Given the performance–cost trade-off inherent to Nd–Fe–B, we frame our optimization problem as a constrained one, where novel compositions are searched in a sub-space within pre-specified cost constraints (where the costs are calculated based on the market price of the doping species), in order to guide the search toward an improved performance–cost ratio. Our workflow is illustrated in Fig. 1. Starting from an initial dataset of 24 compositions, with varying doping wt% of La, Ce, Y, Co, and Ni, we constructed ML surrogate models to map ML-identified atomic descriptors to the magnetic properties of Nd–Fe–B. An ensemble of 100 SVR models demonstrated the best predictive capability, and was hence used to make recommendations for new compositions in an iterative way. With multiple optimization goals in mind, we updated our model sequentially to first identify compositions with improved HT $B_r$ (Stage 1) and furthermore compositions with overall performance, taking into account both $B_r$ and $H_{cj}$ (Stage 2).

# 2 Dataset

## 2.1 Description

Our initial dataset comprises of 24 compositions, with a nominal composition of $(Nd_{80}Pr_{20})_{30.80-x-y-z}La_xCe_yY_z$-$Fe_{66.67-u-w}Co_uNi_wB_{0.96}M_{1.57}$ (M = Al, Cu, Ga, Ti, in wt%), where $x$, $y$, $z$, $u$, and $w$ represent the substitution level (wt%) of La, Ce, Y, Co, and Ni, respectively. We refer to the composition without any of the doping species ($x = y = z = u = w = 0$) as pristine Nd–Fe–B. La, Ce, and Y are introduced to substitute the $Nd_{80}Pr_{20}$ alloy as a whole.

## 2.2 Experimental details

The alloys (compositions) were prepared with strip casting, and then subjected to hydrogen decrepitation to get a coarse powder, and jet milled in a nitrogen atmosphere to produce a fine powder with an average grain size of ~3.5 μm. The as-prepared powder was then aligned and pressed in a magnetic field of 2 T, followed by isostatic compacting under a pressure of 150 MPa. The resulting compacts were further sintered at 1030–

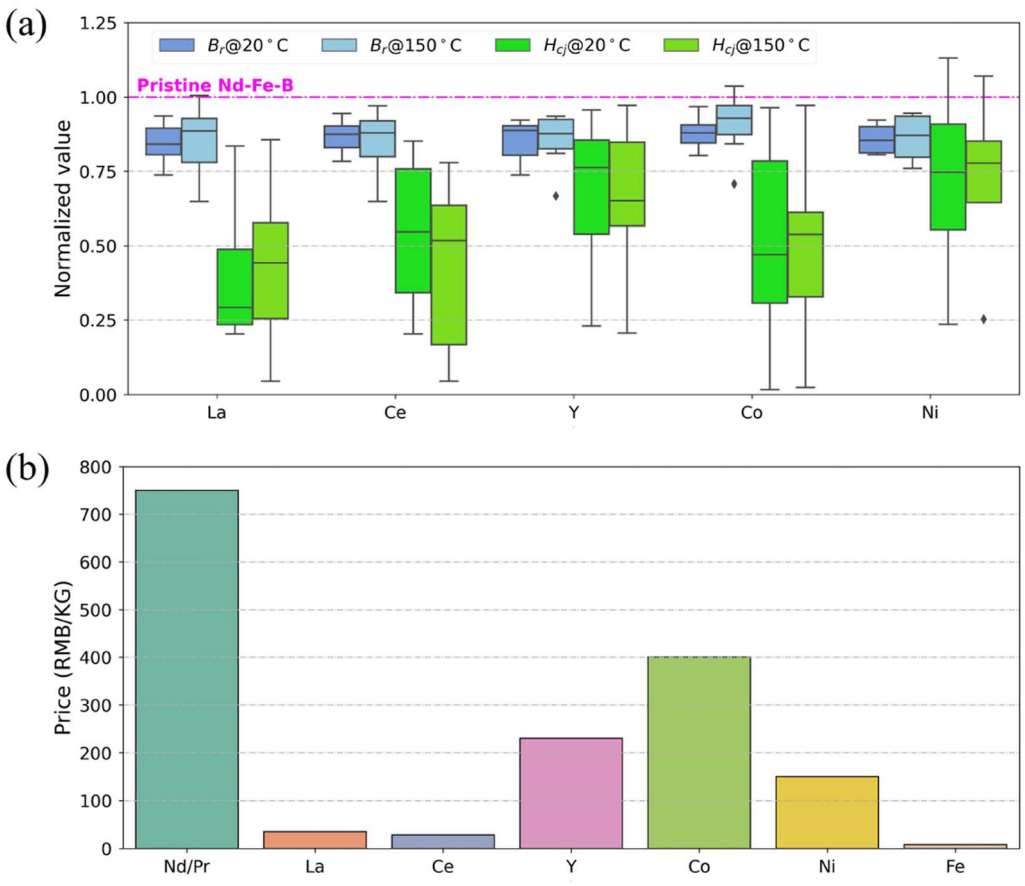


Fig. 2 (a) Distribution of magnetic properties for different doping species in the initial dataset, normalized with that of pristine Nd-Fe-B. The average value is represented with a black line in each panel; (b) prices of the doping species in units of RMB/KG, where Nd/Pr represents the $Nd_{80}Pr_{20}$ alloy used as the raw material for fabricating the samples. The values are tabulated in ESI† Table S2.

1060 °C for 6–8 h in vacuum, and then annealed at 800–850 °C for 2–4 h and 450–520 °C for 3–5 h, to produce the final magnets. Magnetic property measurements were performed using a DC BH Curve Tracer (National Institute of Metrology, NIM-2000). Microstructure observations were conducted using a scanning electron microscope (SEM). Elemental concentration was measured using an electron probe microanalyzer (EPMA), where the values were obtained by averaging over five measurements in the interior of five different grains.

### 2.3 Magnetic performance

The initial dataset comprises 24 compositions, including pristine Nd–Fe–B, 7 compositions with one doping species, 12 compositions with two doping species, and 4 compositions with three doping species, as tabulated in ESI† Table S1. These systems are referred to as pristine, unary, binary and ternary (doping) systems in the following discussion. The magnetic properties ($B_r$&$H_{cj}$) of the samples in the initial dataset are shown in Fig. 2a, normalized with that of pristine Nd–Fe–B, and the prices of the doping species are shown in Fig. 2b, with respect to that of the host species (Nd/Pr and Fe). The variation observed in $H_{cj}$ is much more significant than that of $B_r$. The value of $B_r$ invariably decreases, with the doping of all five species, with the exception of $B_r$@150 °C, where higher values than that of pristine Nd–Fe–B could be achieved at a high doping wt% of Co (18% on closer inspection of the initial dataset). Similarly, a decrease in $H_{cj}$ is observed for all the doping species except Ni. The performance of Nd–Fe–B with dopants is directly correlated with its cost: La/Ce/Y are less expensive than Nd/Pr, and hence are required if cost reduction is the objective, yet they are detrimental to $B_r$&$H_{cj}$ as doping species; Co/Ni could be the pathway toward elevated $B_r$&$H_{cj}$ of Nd–Fe–B, especially at HT, yet they are much more expensive than Fe. Although the combination of these species could potentially lead to a greater performance–cost ratio, it is challenging to find such a combination due to the vast composition space involved.

### 2.4 Partitioning behavior

It is well-known that when a certain amount of La/Ce, *etc.* is doped into the Nd–Fe–B system, not all of the doping species enter the main phase. Instead, a significant portion of them enters the grain boundary region, forming RE-rich grain boundary phases along with Nd/Fe, such as $REFe_2$, $RE(Fe,Co)_4B$, *etc*[33]. This partitioning behavior, namely, the partitioning of a doping species in the $Nd_2Fe_{14}B$ main phase and Nd-rich grain boundary phase, has significant implications for the magnetic property of the resulting Nd–Fe–B.[68,69] Leveraging our current dataset with 24 samples spanning a wide range of nominal wt%, we first investigate the partitioning behavior of the five different doping species. The wt% of the doping species in the main phase was measured with Joel EPMA, and is termed main phase wt%. The tendency of a doping species to enter the main phase, hence, could be evaluated by taking the ratio of the main phase wt% and nominal wt% ($R_m$). The results are shown in Fig. 3. For each doping species each point corresponds to a particular sample where the concerned doping species is present. As indicated by the dashed line, a clear linear trend is

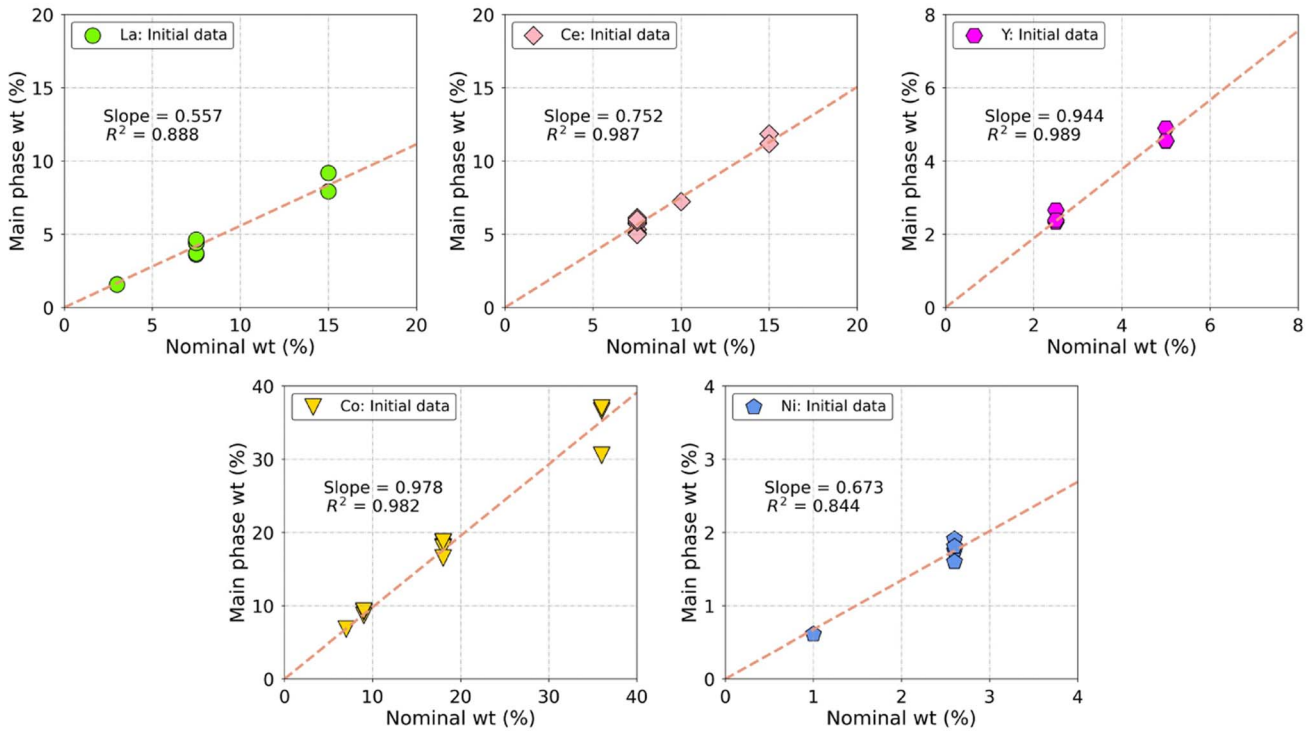


Fig. 3 Variation of main phase wt% *vs.* nominal wt% for the five doping species, based on the initial dataset of 24 samples. A linear fit renders a slope (intercept is forced to be 0), representing the average ratio of main phase wt% and nominal wt%.

 

observed for all the doping species, suggesting that they all demonstrate a stable partitioning behavior over the range of wt% covered here. As such, $R_m$ is calculated as the slope of the linear fit to the data points (with intercept set to zero), and is found to be 0.569 for La, 0.755 for Ce, 0.944 for Y, 0.976 for Co, and 0.677 for Ni. Hence, La/Ce/Ni only partially enters the main phase, where the majority of Y/Co is observed. To our knowledge, this is the first systematic study of the partitioning behavior of the above doping species in Nd–Fe–B.

In this work, we choose to optimize over main phase wt%. It is worth noting that, assuming the validity of the above linear partitioning trend within the range of wt% covered here, it makes little difference whether one chooses to optimize over the nominal wt% or the main phase wt%. As will be further shown, this linear trend holds as well for the augmented dataset with the 9 newly predicted compositions in the following adaptive iterations (see ESI† Fig. S1). Therefore, all compositions henceforth will be specified based on main phase wt% of the above doping species, unless otherwise noted.

# 3 Methods

Six different ML algorithms were used in this work: gaussian process regression (GP), support vector regression (SVR), ridge regression (RR), K-nearest neighbors regression (KNN), artificial neural network (ANN) and decision tree (DT), as implemented in the Scikit-learn package.[70]

## 3.1 Partitioning behavior

For building a surrogate model for $B_r$&$H_{cj}$, a simple treatment is to use raw features, namely, composition as input features (Approach 1: composition-based fingerprinting). This treatment naturally gave rise to 5 input features: $w_{La}$, $w_{Ce}$, $w_Y$, $w_{Co}$, and $w_{Ni}$, corresponding to the doping wt% of the five doping species. A more involved approach is to incorporate atomic features that are known to affect $B_r$&$H_{cj}$ (Approach 2: domain-knowledge-based fingerprinting). We considered 16 different atomic features for each species (a full list of descriptors, along with the corresponding values are tabulated in ESI† Table S3). These fingerprints encode the general atomic information (such as atomic number and radii), atomic properties (such as electronegativity, valence electron number, ionization potential, *etc.*) of the rare-earth elements (denoted with suffix R) and transition metals (denoted with suffix T). All these features, except the last two: Curie temperature ($T_C$) and saturation magnetization ($\mu$), were retrieved from ref. [71] For the last two features ($T_C$ and $\mu$), the value of the rare-earth elements ($Tc_R$ and $\mu_R$) corresponds to that of the associated $Re_2Fe_{14}B$ compounds, whereas the value of the transition-metal elements ($Tc_T$ and $\mu_T$) corresponds to that of the bulk metal only.[2]

As La/Ce/Y are doped into the Nd site (R site), and Co/Ni into the Fe site (T site) in Nd–Fe–B, they were treated separately as two groups. Using atomic number ($Z$) as an example, we obtained a weighted average of atomic number for the R site $Z_R$ based on the wt% of La/Ce/Y (see eqn (1)), and similarly a weighted average of atomic number for the T site $Z_T$ (see eqn (2)). In addition, the product of the above two weighted average was also taken as an extra feature, as a means to capture the interaction of the R site and T site doping elements (see eqn (3)). We therefore arrived at $16 \times 3 = 48$ input features here.

$$Z_R = \sum_{i \in \{La,Ce,Y\}} w_i \times Z_i \quad (1)$$

$$Z_T = \sum_{j \in \{Co,Ni\}} W_j \times Z_j \quad (2)$$

$$Z_{RT} = Z_R \times Z_T \quad (3)$$

## 3.2 Design space

The design space is shown in Table 1, where the doping amount (main phase wt%) of the five doping elements is allowed to vary within a corresponding domain, with a specific interval/resolution. This design space comprises of >200 000 possible compositions. For each composition in the design space, the corresponding nominal wt% was inferred based on $R_m$ of the doping species (as detailed in Section 2.3), and the cost of the composition could then be calculated based on the nominal wt%.

## 3.3 Feature engineering

Starting from 48 preliminary input features obtained with Approach 2, we employed correlation coefficient and recursive feature elimination (RFE) to remove irrelevant and redundant features, as well as to down-select a key feature subset that demonstrated high predictive capability. Leave-one-out cross-validation root-mean-squared-error (LOOCV RMSE error, or LOOCV error) was adopted as elimination criteria in the RFE process. The results were compared with that of Approach 1. Among all the above ML techniques, SVR achieved the lowest LOOCV error for both $B_r$@20 °C and $B_r$@150 °C, and was therefore chosen as the machine learning framework for building our surrogate model (see ESI† Note 1 for details). The 6-feature set generated for SVR is: [$\mu_{RT}$, $Tc_T$, $Tc_{RT}$, $IP_T$, $IP_{RT}$, $Ev_R$], among which $\mu_{RT}$ reflects the effects of the magnetization of doping elements on the $B_r$@20 °C, and $Tc_T$ and $Tc_{RT}$ reflect the effects of the $Tc$ of doping elements, which directly impacts $B_r$@150 °C. These features were also favored by the other machine learning techniques, as shown in ESI† Table S4. The surrogate models in this work were built based on a set of relevant atomic-level descriptors, motivated by previous studies

Table 1 Composition domain (wt%) of the design space, and the corresponding interval/resolution

| Element | Domain | Interval (resolution) |
|---|---|---|
| La | [0,10] | 1 |
| Ce | [0,10] | 1 |
| Y | [0,5] | 0.5 |
| Co | [0,20] | 1 |
| Ni | [0,3] | 0.25 |

which demonstrated that, as compared to using composition alone, incorporation of domain knowledge renders the search more efficient at guiding composition optimization.[72] Expectedly, the benefit of doing so should be greater when the data are scarce, as is our case.[53,73]

### 3.4 Bootstrapping & model construction

Bootstrapping was used for providing estimates of uncertainty. An ensemble of models was trained individually on a corresponding number of subset samples (namely, bootstrap samples that were drawn with replacement from the training set), where the ensemble outputs in itself formed a statistical distribution of the final output, enabling the estimation of the mean and the associated uncertainty (standard deviation). As the SVR model showed the lowest LOOCV error, we built an ensemble of 100 SVR models as our surrogate model for predicting $B_r$&$H_{cj}$, where 5-fold CV was used to optimize the hyperparameters.

### 3.5 Acquisition function

The obtained surrogate model was used to scan a design space, and make predictions, namely, mean ($\mu$) and uncertainty ($\sigma$), for all the compositions in the design space, and furthermore to recommend compositions that maximize an acquisition function under a cost constraint. We used upper confidence bound (UCB): $f = \mu + k \times \sigma$ with $k = 1$ as our acquisition function. There are several other well-known acquisition functions, among which expected improvement (EI) has been extensively used for adaptive learning.[57,72,74,75] Our optimization is bounded by the trade-off that compositions with lower cost are usually associated with the reduced achievable $B_r$&$H_{cj}$. The use of EI as the acquisition function would indiscriminately render EI values that are close to zero for all the compositions below a certain cost bound, and hence, is undesirable as an acquisition function for such a cost bound. We therefore resorted to UCB here, which did not suffer from this drawback (see ESI† Note 2 for more details on EI and UCB, and our rationale for choosing UCB over EI). Three different cost constraints (w.r.t. pristine Nd–Fe–B with a cost of ~236 RMB/KG) were applied: C1: ~0% cost reduction (also referred to as similar cost hereafter), C2: ~10% cost reduction, C3: ~20% cost reduction (see ESI† Note 3 for more details on cost constraints). The as-trained surrogate model was then used to recommend one composition under each of the above three cost constraints, totaling three compositions. Nd–Fe–B samples with the recommended composition were then fabricated, characterized, compared to our predictions, and then added to the current training set to update/modify the model iteratively.

### 3.6 Optimization goal

Our adaptive-learning flow consists of two stages, wherein different optimization goals are involved in each stage:

Stage 1. Surrogate models were constructed to predict $B_r$@150 °C, and recommendations for new samples were made

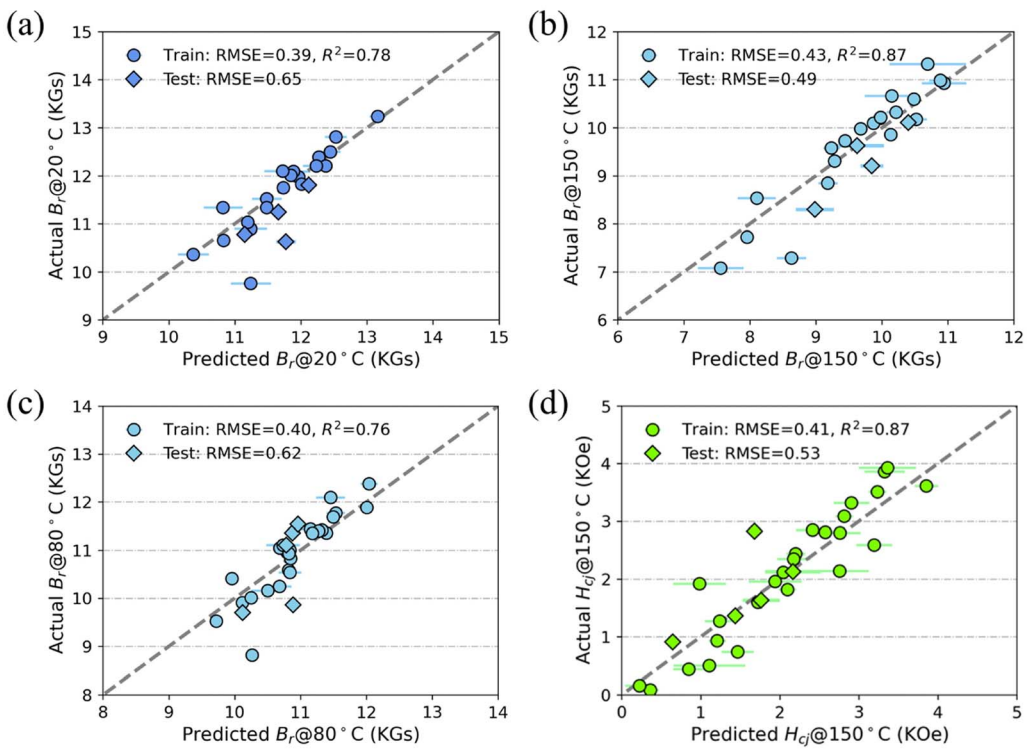


Fig. 4 Parity plot of (a) $B_r$@20 °C, (b) $B_r$@150 °C showing the performance of the SVR surrogate model on the initial dataset (to kick-start Stage 1); parity plot of (c) $B_r$@80 °C, (d) $H_{cj}$@150 °C showing the performance of the SVR surrogate model on the augmented dataset (to kick-start Stage 2). The model-predicted range ($\mu \pm \sigma$) is shown as horizontal error bars centered at the predicted mean ($\mu$), spanning a width double the predicted uncertainty ($\sigma$).

 

to maximize $B_r$@150 °C. The goal was to identify compositions with exceptional HT $B_r$.

Stage 2. Surrogate models were constructed to predict $B_r$@80 °C and $H_{cj}$@150 °C, and recommendations for new samples were made to maximize a measure of overall performance, $M_{B_r\&H_{cj}}$, defined as the product of $B_r$@80 °C and $H_{cj}$@150 °C, given the trade-off between $B_r$ and $H_{cj}$. The goal was to identify compositions with exceptional overall performance.

Although excellent $B_r$@150 °C is desirable, we switched our optimization goal for $B_r$ to $B_r$@80 °C in Stage 2 as 80 °C is the most typical (frequent) operating regime of Nd–Fe–B-based permanent magnets in electric motors used in the automotive industry. Therefore, a higher $B_r$@80 °C is of critical importance for such applications, which we are interested in.

# 4 Results: adaptive learning

## 4.1 Model performance

The parity plots in Fig. 4 show the performance of the surrogate models on the train and test sets for Stage 1 (Fig. 4a and b) and Stage 2 (Fig. 4c and d), where the horizontal error bars represent the uncertainty of the prediction evaluated through bootstrapping. Generally, the model tends to under-estimate $B_r\&H_{cj}$ at the high end, which is typically observed in other studies.[74,76,77] It is noted here that, as the optimization goal was altered in Stage 2, a new RFE process was initiated with the initial dataset and augmented data from Stage 1 (see ESI† Fig. S4 for details).

## 4.2 Iterative design

Two iterations were conducted in Stage 1. The recommended compositions and the associated $B_r$@150 °C are shown in Fig. 5a (iteration 1) and 5b (iteration 2), along with the experimentally measured values. For the sake of comparison, the initial dataset is also plotted and shown as iteration 0 (with pristine Nd–Fe–B highlighted as a cross). In particular, it is noted here that among all the compositions in the initial dataset, only two demonstrate higher $B_r$@150 °C than pristine Nd–Fe–B, yet at the same time much higher cost due to the high wt% of Co (see ESI† Table S1). The recommended samples are labeled 1: C1, 1: C2, 1: C3 for iteration 1, subject to the corresponding cost constraint as discussed before, and

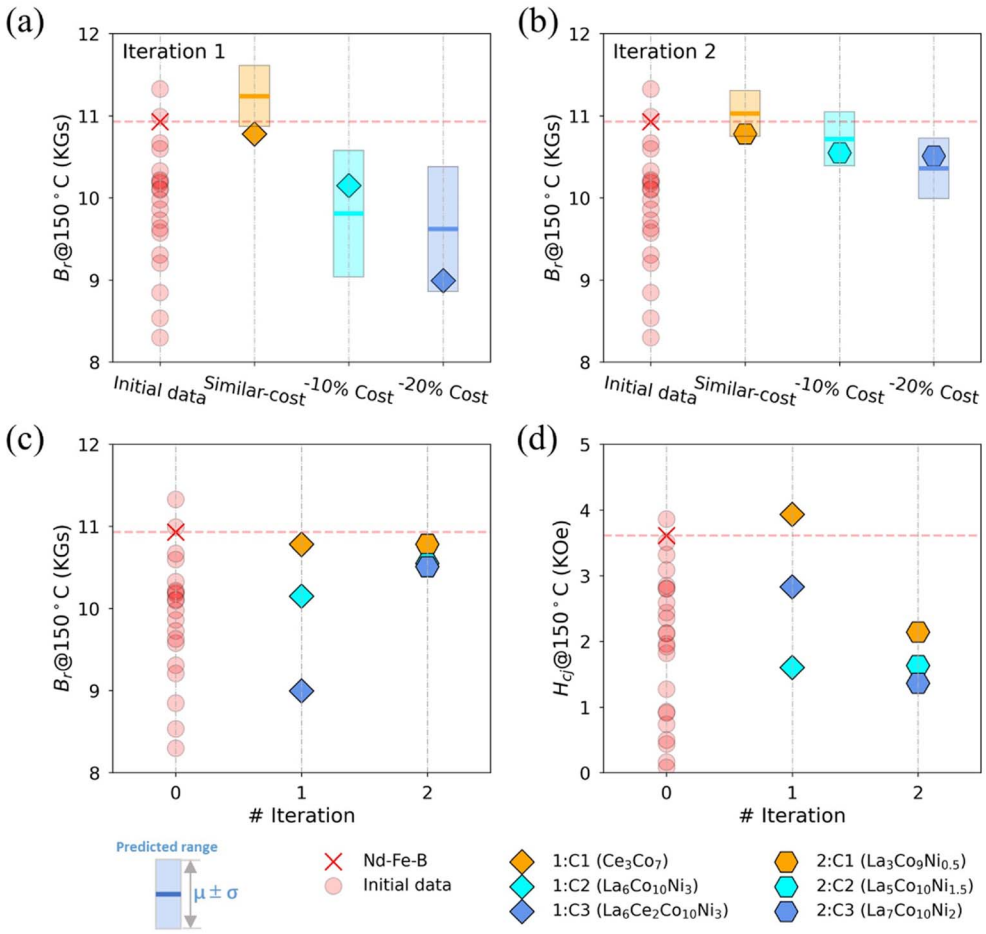


Fig. 5 Recommended compositions and their corresponding $B_r$@150 °C in (a) iteration 1, (b) iteration 2. Variation of (c) $B_r$@150 °C, (d) $H_{cj}$@150 °C over iterations, with the initial dataset shown as iteration 0. In (a) and (b) model-predicted range ($\mu \pm \sigma$) is shown as vertical bars centered at the predicted mean ($\mu$), spanning a height double the predicted uncertainty ($\sigma$), and the measured values are shown as diamonds for iteration 1 and hexagon for iteration 2. In (a–d) dashed horizontal lines are included to show the value for pristine Nd–Fe–B as a benchmark. The compositions are specified based on the main phase wt% of the associated doping species.

similarly 2: C1, 2: C2, 2: C3 for iteration 2. The surrogate model recommended a Ce/Co binary system ($Ce_3Co_7$) during iteration 1 (Fig. 5a), with $B_r$@150 °C close to pristine Nd–Fe–B. The other two compositions recommended in Stage 1 (1: C2, 1: C3) showed relatively low $B_r$@150 °C. During iteration 2, the model made recommendations of the La/Co/Ni ternary system exclusively, and the corresponding $B_r$@150 °C all surpassed 10.5 KGs, which was only ~0.4 KGs lower (~4% lower) than pristine Nd–Fe–B (Fig. 5b). Notably, 2:C3 ($La_7Co_{10}Ni_2$), with ~40% of Nd/Pr replaced by La, achieved a $B_r$@150 °C of 10.51 KGs, at a cost reduction of ~20%.

To better compare the performance of recommended compositions, the variations of $B_r$@150 °C and $H_{cj}$@150 °C over iterations are plotted in Fig. 5c and d, respectively. The recommended compositions in iteration 2 generally showed increased $B_r$@150 °C over those in iteration 1, expectedly so as it is the target property in Stage 1. However, this is also accompanied by a general decrease in $H_{cj}$@150 °C, as shown in Fig. 5d. The above La/Co/Ni ternary system in iteration 2, $La_7Co_{10}Ni_2$ for example, despite a high $B_r$@150 °C at ~20% reduced cost (Fig. 5c), is not suitable for HT applications, due to its low $H_{cj}$ (Fig. 5d). As is evident from Fig. 5d, except for the Ce/Co binary system $Ce_3Co_7$, all the other La/Co/Ni ternary systems showed low $H_{cj}$@150 °C, well below that of pristine Nd–Fe–B. Among all the 6 recommended compositions, only $Ce_3Co_7$ showed improved overall HT performance compared to that of pristine Nd–Fe–B, with a ~8.9% enhancement in $H_{cj}$@150 °C and ~1.4% reduction in $B_r$@150 °C, at a similar cost. Detailed values for all the recommended compositions are shown in ESI† Table S5.

To improve the overall performance, the recommendations in Stage 2 were made to maximize $M_{B_r\&H_{cj}}$. The recommended compositions and the associated $B_r$@80 °C, $H_{cj}$@150 °C and $M_{B_r\&H_{cj}}$ are shown in Fig. 6a–c, along with the experimentally measured values. The values are shown for all the compositions in the initial dataset (with pristine Nd–Fe–B highlighted as a cross), as well as the 9 extra compositions recommended in Stage 1 and Stage 2. Merits of the recommended samples are also benchmarked against pristine Nd–Fe–B, the composition with the highest $M_{Br\&Hcj}$ in the initial dataset (Fig. 6c). As compared to the first two iterations in Stage 1, the recommended compositions here demonstrate reasonably high $B_r$@80 °C (Fig. 6a), and importantly, much higher $H_{cj}$@150 °C (Fig. 6b). Note that the first two compositions recommended here, 3: C1 ($Ce_1Co_1$) and 3: C2 ($La_1Ce_1Ni_{0.25}$) both showed a higher $H_{cj}$@150 °C than the pristine Nd–Fe–B, albeit with slightly lower $B_r$@80 °C. The resulting $M_{B_r\&H_{cj}}$ of these two compositions are hence much higher than those of the pristine Nd–Fe–B, at a similar cost, and ~10% reduced cost, respectively. Fig. 6d shows a scatter plot demonstrating the distribution of $B_r$@80 °C and $H_{cj}$@150 °C where variation of $M_{B_r\&H_{cj}}$ is represented by the dashed gray contour lines. The majority of

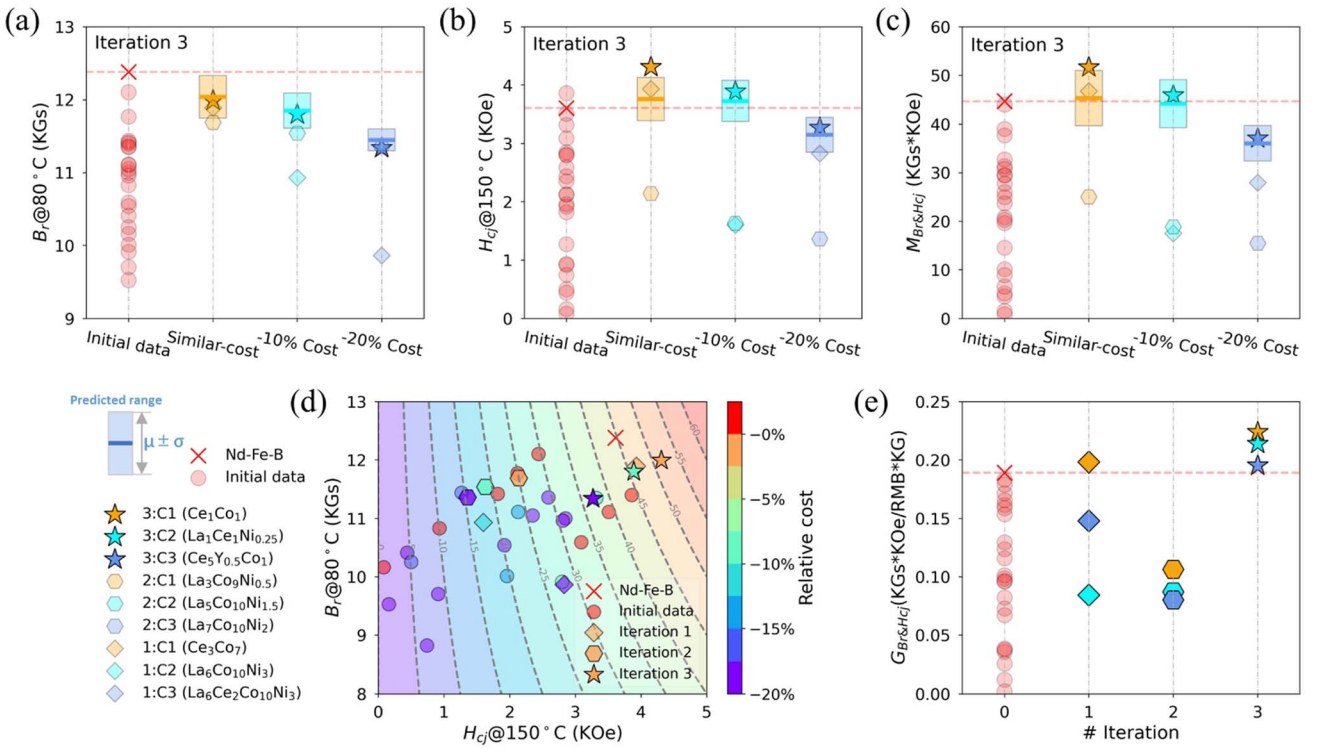


Fig. 6 Recommended compositions and their corresponding (a) $B_r$@80 °C, (b) $H_{cj}$@150 °C, (c) $M_{B_r\&H_{cj}}$ in iteration 3. (d) Contour plot showing the performance of recommended compositions as compared to the initial dataset (with pristine Nd–Fe–B highlighted as a cross), with symbols colored based on the relative cost of the corresponding compositions w.r.t. pristine Nd–Fe–B. The dashed gray contour lines represent the variation of $M_{B_r\&H_{cj}}$. (e) Variation of $G_{B_r\&H_{cj}}$ over iterations, with the initial dataset shown as iteration 0. In (a–c) the model-predicted range ($\mu \pm \sigma$) is shown as vertical bars for iteration 3, similar to that in Fig. 5. The compositions are specified based on the main phase wt% of the associated doping species.

 

the compositions recommended in Stage 1 (iteration 1, 2) demonstrated low $M_{B_r\&H_{cj}}$, except for 1: C1 (orange diamonds). This arises from the low $H_{cj}$ of these samples, as Stage 1 was concerned with maximizing $B_r$@150 °C only. The performances of the three compositions recommended in iteration 3 in Stage 2 (indicated with stars) surpassed those in the initial dataset as well as those in Stage 1, at a similar cost level (indicated by similar color of points in Fig. 6d). It is also worth noting that composition 3: C2 (indicated with cyan stars), at ~10% reduced cost, achieved $M_{B_r\&H_{cj}}$ greater than that of pristine Nd–Fe–B. Detailed values for all the recommended compositions are shown in ESI† Table S6, and demagnetizing curves of the first two compositions recommended in iteration 3 : 3: C1 ($Ce_1Co_1$), 3: C2 ($La_1Ce_1Ni_{0.25}$) are shown in ESI† Fig. S5.

Putting compositions at different cost levels on the same footing, the merits of the compositions were further evaluated based on the performance–cost ratio $G_{B_r\&H_{cj}}$, calculated as $M_{B_r\&H_{cj}}$/cost, as shown in Fig. 6e, where pristine Nd–Fe–B demonstrated the highest of $G_{B_r\&H_{cj}}$ in the initial dataset. A performance–cost ratio gain, $\Delta G_{B_r\&H_{cj}}$, defined as percentage gain in $G_{B_r\&H_{cj}}$ w.r.t. pristine Nd–Fe–B, was found to be negative (or zero) for all the compositions in the initial dataset, whereas 4 out of 9 compositions recommended demonstrated positive $\Delta G_{B_r\&H_{cj}}$. These four compositions are shown in Table 2. Notably, the first two compositions in iteration 3 demonstrated the highest $\Delta G_{B_r\&H_{cj}}$ of 18.4% (3: C1) and 13.1% (3: C2), and are therefore promising candidates for cost-effective Nd–Fe–B PMs. These compositions demonstrate excellent performance at RT as well, as shown in ESI† Fig. S6, although it was not as significant as that observed at HT, as discussed above. In addition, the recommended compositions with high $G_{B_r\&H_{cj}}$ showed excellent temperature coefficients of $B_r$ ($\alpha_{B_r}$) and $H_{cj}$ ($\beta_{H_{cj}}$) at 150 °C as well (see ESI† Note 4), for example, improved $\beta_{H_{cj}}$ over pristine Nd–Fe–B, as shown in ESI †Fig. S7. Therefore, excellent RT performance, along with improved temperature stability, contributed to the improved HT performance of these recommended compositions.

# 5 Discussion

## 5.1 Post-hoc interpretation

Closer inspection of the recommended compositions and the predicted values indicates a transition from exploration to exploitation from iteration 1 to 3. For example, inspection of the Ni wt% of the recommended compositions reveals that 1: C2 and 1: C3 in iteration 1 featured a Ni wt% (3 wt%) beyond the range covered in the initial dataset (0–1.9 wt%), and thus was extrapolative in nature, and this was not the case in iteration 2–3 (w.r.t. the augmented dataset). The predicated uncertainty ($B_r$ values, for example) w.r.t. that of the predicted values (mean) decreased from iteration 1 to 3, indicative of a transition from uncertainty-driven (explorative) to mean-driven (exploitative) search strategy, as more data were accumulated and the model became more 'confident' (and less 'uncertain') in its prediction, as illustrated in ESI† Fig. S8.[55,65] In addition, the selection strategy of the trained model, namely, characteristics of the recommended compositions, was driven by the associated optimization goal. Fig. 7 shows the distribution of wt% of La and Ce for recommended compositions. The model demonstrated a manifest preference for La as Nd-site doping species in Stage 1, with 5 out of 6 recommended compositions being entirely or primary La, as observed in Fig. 5. Hence, the selection strategy was La-oriented in Stage 1, where the optimization of $B_r$@150 °C was the goal. Notably, all the 3 compositions recommended in iteration 2 were La/Co/Ni ternary systems, indicating the model's strong "belief" in the superior $B_r$@150 °C of the La/Co/Ni system, which was also borne out by the experimental results. Here the choice of La over Ce as the Nd-site doping species could be attributed to the higher $T_C$ of $La_2Fe_{14}B$ (530 °C) than that of $Ce_2Fe_{14}B$ (424 °C),[2] which contributed to improved temperature stability and hence higher $B_r$@150 °C. These La-oriented systems, however, demonstrated very low $H_{cj}$, as shown in Fig. 5d. When the optimization goal shifted from $B_r$@150 °C in Stage 1 to $M_{B_r\&H_{cj}}$ in Stage 2, the selection strategy shifted from La-oriented to Ce-oriented, as indicated by the dominance of Ce in the 3 recommended compositions in iteration 3 (Fig. 6). $H_{cj}$ of these Ce-oriented compositions, both at RT and HT, was much higher than that of La-oriented ones in Stage 1 (see Fig. 6 and ESI† Fig. S6).

To understand the microstructural origin of the improved $H_{cj}$ of compositions in iteration 3, back-scattered SEM images of the recommended compositions of iteration 2 and iteration 3 are shown in Fig. 7. Clearly, Ce-oriented compositions showed thicker and more uniform grain boundaries (Fig. 7d–f) than the La-oriented compositions (Fig. 7a–c). This distinct difference in the microstructure of the Ce-oriented and La-oriented systems is believed to be responsible for the higher $H_{cj}$ of the former.[78] In contrast to La and Ce, Y was rarely recommended by the model, except in 3: C3 ($Ce_5Y_{0.5}Co_1$), where only ~0.5 wt% Y was included. Although Y was known to improve the temperature stability of $Nd_2Fe_{14}B$, the observed improvement was found to be insufficient to justify its presence. The variation of $B_r\&H_{cj}$ with the wt% of La, Ce and Y as predicted by the model (Stage 2) is shown in ESI† Fig. S9, where the model identified Y to be much more detrimental to the magnetic properties of Nd–Fe–B than Ce at both RT and HT, which, coupled with the higher cost of Y over La and Ce, could help explain why the model favored the latter two over Y.

Notably, at ~10% reduced cost, the superior performance of 3: C2 ($La_1Ce_1Ni_{0.25}$) is believed to arise partially from the presence of Ni as well. Ni could potentially benefit Nd–Fe–B in two aspects: (1) Ni possesses a higher $T_C$ than Fe, and hence benefits

Table 2 Compositions with positive performance–cost ratio gain $\Delta G_{B_r\&H_{cj}}$ in the entire dataset. The compositions are specified based on the main phase wt% of the associated doping species

| Iteration | Main phase wt% | Relative cost | $G_{B_r\&H_{cj}}$ | $\Delta G_{B_r\&H_{cj}}$ |
|---|---|---|---|---|
| 1: C1 | $Ce_3Co_7$ | 0% | 0.189 | 4.8% |
| 3: C1 | $Ce_1Co_1$ | −2.4% | 0.198 | 18.4% |
| 3: C2 | $La_1Ce_1Ni_{0.25}$ | −9.2% | 0.224 | 13.1% |
| 3: C3 | $Ce_5Y_{0.5}Co_1$ | −19.7% | 0.195 | 3.3% |

$ß_{H_{cj}}$ as well as $\alpha_{B_r}$, resulting in the improved HT performance of Nd–Fe–B, similar to that of Co; (2) Ni is found to be able to effectively reduce the grain size of the Nd–Fe–B microstructure, leading to higher $H_{cj}$ and $ß_{H_{cj}}$.[79] For example, $ß_{H_{cj}}$ of 3: C2 ($La_1Ce_1Ni_{0.25}$) at 150 °C is −0.590% per °C, which is superior to the value of −0.600% per °C for pristine Nd–Fe–B (ESI† Fig. S7). In addition, the measured grain size of 3: C2 ($La_1Ce_1Ni_{0.25}$) is 4.13 ± 0.16 μm, appreciably smaller than that of pristine Nd–Fe–B (4.69 ± 0.19 μm), suggesting the effectiveness of Ni at grain size reduction, even at a low wt% of 0.25%. However, Ni is detrimental to RT $B_r$ at the same time. The superior performance of 3: C2 is believed to arise primarily from an optimal wt% of Ni, balancing $B_r$, $H_{cj}$ and cost.

Previous studies have shown Ce/Co to be a promising doping combination for achieving Nd–Fe–B PMs with excellent performance, due to the synergistic effects of Ce and Co.[22,32] This was "recognized" by the model, which recommended two Ce/Co systems: 1: C1 ($Ce_3Co_7$) and 3: C1 ($Ce_1Co_1$), with the latter demonstrating the highest $M_{B_r\&H_{cj}}$ and $G_{B_r\&H_{cj}}$ among all the compositions. These Ce-oriented compositions demonstrated much higher $H_{cj}$@150 °C than La-oriented ones, yet at the same time lower $B_r$@150 °C (see ESI† Fig. S10). The above observation hence points to a trade-off between $B_r$@150 °C and $H_{cj}$@150 °C. Hence, it is unlikely that simultaneous enhancement of $B_r$ and $H_{cj}$ could be achieved through doping with the investigated species in this work, although it can be achieved with a grain boundary diffusion process[80] or through an annealing process.[81]

### 5.2 Performance–cost relationship

The obtained model could be used to gain insight on the performance–cost relationships for Nd–Fe–B samples. Fig. 8a and c show the performance *vs.* cost over the entire design space based on model prediction for $B_r$@80 °C and $H_{cj}$@150 °C (Stage 2), respectively. A few observations are made here. (1) There is a spread of about ∼2 KGs for $B_r$@80 °C and ∼2 KOe for $H_{cj}$@150 °C at a fixed cost, which is an indication that substantial and nearly fixed improvement could be attained at different levels of cost. (2) The highest $B_r$@80 °C and $H_{cj}$@150 °C that can be achieved through composition optimization decreases with the cost, as indicated by the upper boundary of the spread in the middle region (from C1 to C3). To show this more clearly, points were sampled from the upper boundary at regular intervals (5% of the cost of pristine Nd–Fe–B) and plotted in Fig. 8b and d. A preliminary linear fit in the region bounded by C1 and C3 rendered a slope of 0.324 KGs/10% cost for $B_r$@80 °C and 0.354 KOe/10% cost for $H_{cj}$@150 °C, namely, for each 10% cost reduction (10% of that for pristine Nd–Fe–B, namely, ∼23.6 RMB/KG), the highest achievable $B_r$@80 °C and $H_{cj}$@150 °C are reduced by 0.324 KGs and 0.354 KOe, respectively. The above plots generated with the as-obtained model furnish a glimpse into the performance–cost relationship of Nd–Fe–B in a quantitative way, and provide guidelines as to how much more room for improvement there exists in terms of optimizing the above properties, and importantly, how this varies with the design goal of cost-reduction. In addition, a non-linear trend of the variation is observed in the upper boundary of $B_r$@80 °C and $H_{cj}$@150 °C, and specifically, evidenced by a marginal drop in between C1 and C2, and significant decrease in between C2 and C3, especially for $H_{cj}$@150 °C. Finally, the distribution of the scatter points in Fig. 8a and c suggests that in general, a high amount of Co is unfavorable for achieving high values of $H_{cj}$@150 °C, also evident from the low wt% of Co in the

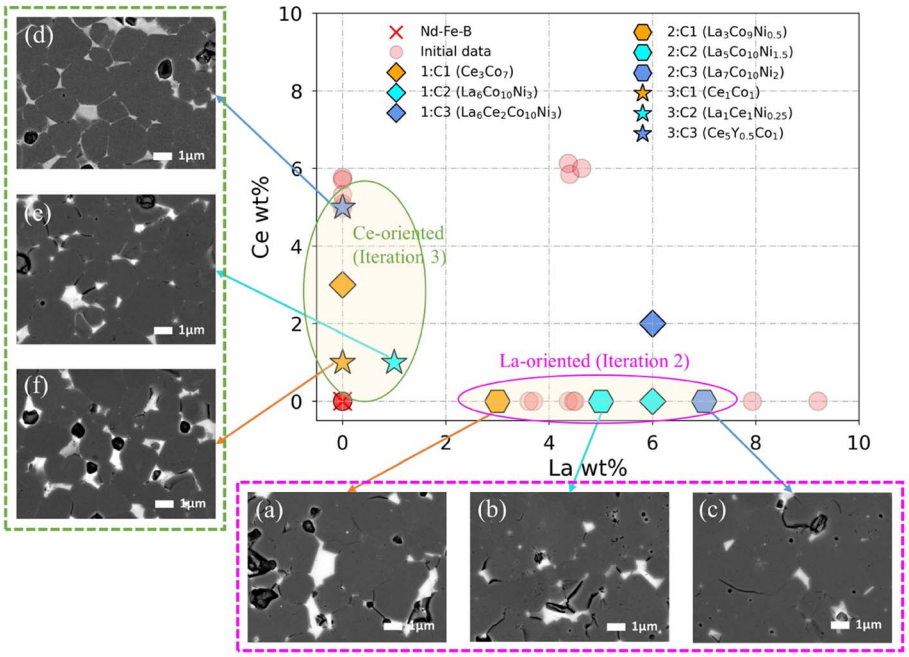


Fig. 7 Distribution of wt% of La and Ce for recommended compositions, along with that of the initial dataset (with pristine Nd–Fe–B highlighted as a cross). Back-scattered SEM image of recommended compositions: (a–c) La-oriented compositions in iteration 2, (d–f) Ce-oriented compositions in iteration 3.

 

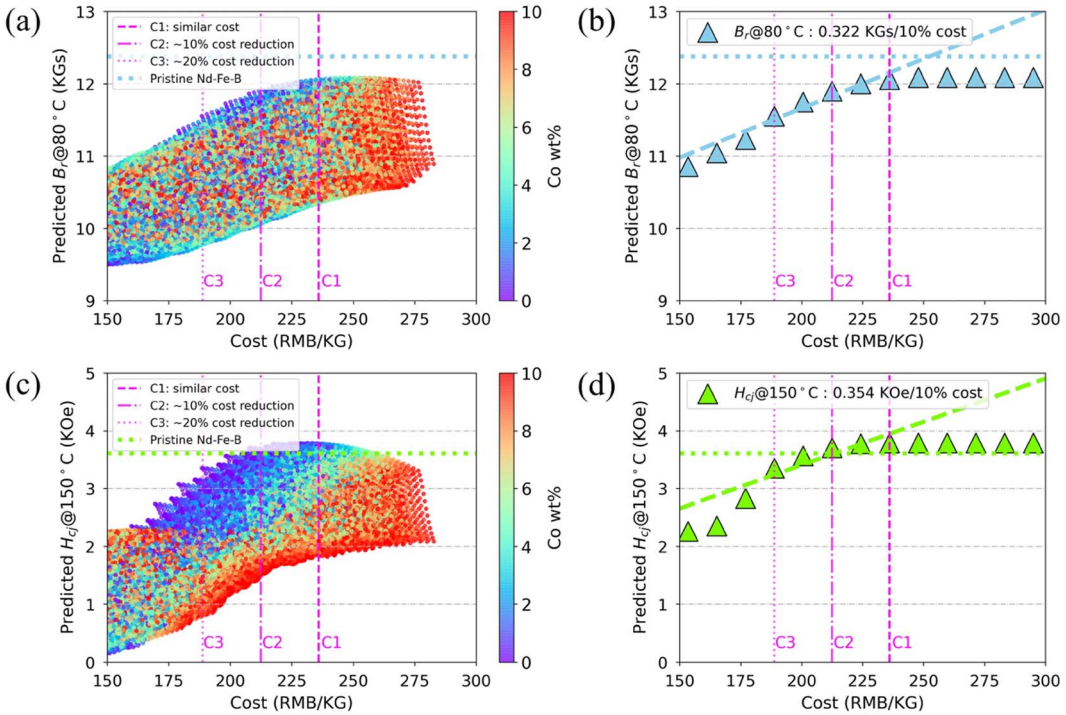


Fig. 8 (a) Scatter plots showing $B_r$@80 °C *vs.* cost over the entire design space based on model prediction, (b) the corresponding upper boundary from (a); similarly, (c) and (d) show the results for $H_{cj}$@150 °C. Points are colored based on Co wt% in (a) and (c). The three levels of cost constraint: C1, C2 and C3 are indicated with perpendicular dashed magenta lines.

compositions recommended in Stage 2 (Fig. 6). This is different from the scenario in Stage 1 (Fig. 5), where optimization of $B_r$@150 °C was the goal and high wt% of Co was recommended invariably. This again points to the trade-off between $B_r$ and $H_{cj}$ for Nd–Fe–B, where the doping wt% of Co was concerned.

### 5.3 Further validation of the model

Here we discuss how our model could be used to gather further insights on the peculiar role of the involved doping species, in light of additional experimental results. First, the effect of Co on $B_r$ is discussed. Fig. 9a and b show the variation of $B_r$@20 °C and $B_r$@150 °C with Co wt% as predicted by the model (Stage 1). As our current dataset only includes Co wt% of 18% for the unary system, we utilize our earlier experimental results of a Co-series that feature a different base composition termed another base here: $B_{0.965}Dy_3\ M_{0.56}$ (M = Al, Cu, Ga, Ti, Zr) as compared to the current base used for model construction. This new base features a different wt% of Al, Ga, B from the current base, and importantly, an additional 3% Dy, among other differences. Note how the pristine Nd–Fe–B sample, with no doping of Co (as indicated by the left-most points in Fig. 9a and b), shows different $B_r$, due to the difference in the base composition as detailed above. Given such a difference in base composition, the main goal here is to examine how our model captured the trends observed in the experiment. The model predicted that a Co wt% below ~5% does not lead to appreciable degradation of $B_r$@20 °C, but is detrimental to $B_r$@20 °C beyond it, as shown in Fig. 9a. This trend predicted by the model was also observed with experimental results on the new base. In addition, as shown in Fig. 9b, the model predicted an increase in $B_r$@150 °C with Co wt%, peaking at ~10%, and a drop beyond it. The above trend agrees with the experimental results up to ~10%, where the values rise up quickly at a low wt% of Co, but show a tendency to plateau at ~10%. As such, although a high Co wt% was generally required to enhance $B_r$@150 °C, as was the case in Stage 1, Co wt% beyond ~10% was not recommended (Fig. 5). This trend is also confirmed by recent studies, and attributed to the transition of the grain boundary phase from the non-magnetic to the ferromagnetic state at a high wt% of Co.[33] The above results demonstrated that the model was able to learn patterns that are general and translate well to other Nd–Fe–B samples with different base compositions. This generality of the learned model is crucial, in suggesting that our model is robust enough to be applicable for a wide range of applications involving Nd–Fe–B materials with varying base. Secondly, we comment on the role of Ce. As shown in Fig. 9c, the decrease in both $B_r$@80 °C and $H_{cj}$@150 °C with Ce wt% as predicted by the model (Stage 2) was shown to be much more significant as Ce wt% goes beyond ~5%. This variation could be attributed to the formation of a secondary $CeFe_2$ phase in the microstructure beyond a critical Ce wt% of ~5%, as shown in Fig. 9d as well as in other published studies.[82] As such, we note here that although our model takes as input the amount of the doping species only and hence is microstructure-agnostic, its predictions, when scrutinized, could still shed light on possible microstructural changes in Nd–Fe–B samples, and hence are helpful towards guiding experimental characterization.

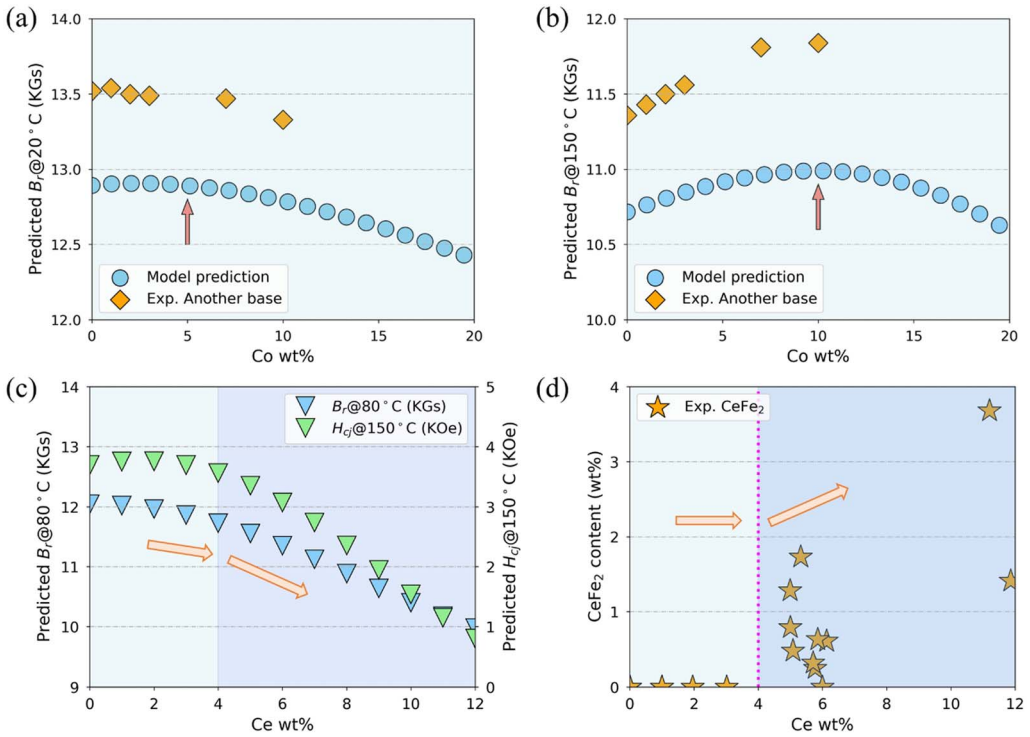


Fig. 9 Variation of (a) $B_r$@20 °C and (b) $B_r$@150 °C with Co wt% as predicted by the model (Stage 1), as compared to that of a series of Co-doped Nd–Fe–B samples with a different base composition as compared to the current base used to construct the model. (c) Variation of $B_r$@80 °C and $H_{cj}$@150 °C with Ce wt% as predicted by the model (Stage 2), (d) variation of wt% of $CeFe_2$ in the sample with Ce wt% for all the samples in the initial dataset.

## 6 Conclusion

We proposed the use of an adaptive-learning framework for accelerated discovery of Nd–Fe–B-based PMs, with La, Ce, Y, Co, and Ni as doping species. It was shown that feature engineering is crucial towards the construction of models with high predictive capability, as compared to using compositions alone as features. Based on a lean set of 24 compositions, the trained surrogate model successfully predicted new compositions with an improved performance–cost ratio over that of the pristine Nd–Fe–B. Our work led to the discovery of several promising compositions: (a) La/Co/Ni ternary systems with excellent HT remanence, (b) Ce/Co binary system and (c) La/Ce/Ni ternary systems with enhanced overall performance ($M_{B_r\&H_{cj}}$), at similar cost and ~10% reduced cost, respectively. These novel compositions were identified through Bayesian Optimization within 3 iterations only, from a vast optimization space with ~200 000 possible candidates, demonstrating the effectiveness of the adaptive-learning approach in accelerated materials discovery. Closer examination of our surrogate model also revealed interesting performance–cost relationships inherent to Nd–Fe–B materials. The generality of the obtained model, as validated with additional experimental results, suggests that the above novel compositions could potentially be transferable to Nd–Fe–B samples with different base compositions. Importantly, as sintered PMs were studied in this work, which is used in industry for scaled-up production, the novel compositions identified in this work could potentially impact the development of new Nd–Fe–B materials for HT applications.

## Conflicts of interest

There are no conflicts to declare.

## Acknowledgements

The authors thank Chen Ling from the Toyota Research Institute of North America for valuable discussions on the adaptive learning framework, as well as for his comments/suggestions on the manuscript.

## References

1 J. M. D. Coey, *Engineering*, 2020, **6**, 119–131.
2 J. F. Herbst, *Rev. Mod. Phys.*, 1991, **63**, 819–898.
3 X. Liao, J. Zhang, J. He, W. Fan, H. Yu, X. Zhong and Z. Liu, *J. Mater. Sci. Technol.*, 2021, **76**, 215–221.
4 Z. Liu, J. He and R. V. Ramanujan, *Mater. Des.*, 2021, **209**, 110004.
5 T. Zhang, W. Xing, F. Chen, L. Zhang and R. Yu, *Acta Mater.*, 2021, **220**, 117296.
6 X. Xianshuang, X. Tang, Y. Du, H. Wu, J. Ju, L. Wu, R. Chen, W. Yin, L. Zhang and A. Yan, *Acta Mater.*, 2022, **232**, 117945.
7 L. Liu, H. Sepehri-Amin, T. Ohkubo, M. Yano, A. Kato, T. Shoji and K. Hono, *J. Alloys Compd.*, 2016, **666**, 432–439.

 

8 J. Li, L. Liu, H. Sepehri-Amin, X. Tang, T. Ohkubo, N. Sakuma, T. Shoji, A. Kato, T. Schrefl and K. Hono, *Acta Mater.*, 2018, **161**, 171–181.
9 L. Liu, H. Sepehri-Amin, T. T. Sasaki, T. Ohkubo, M. Yano, N. Sakuma, A. Kato, T. Shoji and K. Hono, *AIP Adv.*, 2018, **8**, 056205.
10 X. Tang, H. Sepehri-Amin, T. Ohkubo, M. Yano, M. Ito, A. Kato, N. Sakuma, T. Shoji, T. Schrefl and K. Hono, *Acta Mater.*, 2018, **144**, 884–895.
11 T. H. Kim, T. T. Sasaki, T. Ohkubo, Y. Takada, A. Kato, Y. Kaneko and K. Hono, *Acta Mater.*, 2019, **172**, 139–149.
12 X. Tang, J. Li, H. Sepehri-Amin, T. Ohkubo, K. Hioki, A. Hattori and K. Hono, *Acta Mater.*, 2021, **203**, 116479.
13 N. Haque, A. Hughes, S. Lim and C. Vernon, *Resources*, 2014, **3**, 614–635.
14 O. Gutfleisch, M. A. Willard, E. Brück, C. H. Chen, S. G. Sankar and J. P. Liu, *Adv. Mater.*, 2011, **23**, 821–842.
15 J. Cui, M. Kramer, L. Zhou, F. Liu, A. Gabay, G. Hadjipanayis, B. Balasubramanian and D. Sellmyer, *Acta Mater.*, 2018, **158**, 118–137.
16 X. Tang, S. Y. Song, J. Li, H. Sepehri-Amin, T. Ohkubo and K. Hono, *Acta Mater.*, 2020, **190**, 8–15.
17 A.-h. Li, L.-l. Xi, H.-b. Feng, N. Zou, M. Tan, M.-g. Zhu and W. Li, *J. Iron Steel Res. Int.*, 2019, **27**, 1–11.
18 Q. Jiang and Z. Zhong, *J. Mater. Sci. Technol.*, 2017, **33**, 1087–1096.
19 K. Hono and H. Sepehri-Amin, *Scr. Mater.*, 2018, **151**, 6–13.
20 K. P. Skokov and O. Gutfleisch, *Scr. Mater.*, 2018, **154**, 289–294.
21 Y. Liang, Q. Deng, X. H. Tan, H. Li and H. Xu, *Sci. Rep.*, 2019, **9**, 1758.
22 A. K. Pathak, M. Khan, K. A. Gschneidner Jr, R. W. McCallum, L. Zhou, K. Sun, K. W. Dennis, C. Zhou, F. E. Pinkerton, M. J. Kramer and V. K. Pecharsky, *Adv. Mater.*, 2015, **27**, 2663–2667.
23 X. Fan, G. Ding, K. Chen, S. Guo, C. You, R. Chen, D. Lee and A. Yan, *Acta Mater.*, 2018, **154**, 343–354.
24 J.-X. Huang, Y. Liu, J. Li, W. Zhao and Q. Shi, *Rare Met.*, 2019, **39**, 62–69.
25 J. Jin, G. Bai, Z. Zhang and M. Yan, *J. Alloys Compd.*, 2018, **763**, 854–860.
26 Z. Li, W. Q. Liu, Z. P. Zhang, D. Wu, Y. Q. Li and M. Yue, *Mater. Res. Express*, 2020, **6**, 126125.
27 X. F. Liao, J. S. Zhang, H. Y. Yu, X. C. Zhong, L. Z. Zhao, K. Xu, D. R. Peng and Z. W. Liu, *J. Mater. Sci.*, 2019, **54**, 7288–7299.
28 Y. Liu, J. Jin, M. Yan, M. Li, B. Peng, Z. Zhang and X. Wang, *Scr. Mater.*, 2020, **185**, 122–128.
29 W. Lei, Q. Jiang, S. Ur Rehman, L. He, X. Hu, Q. Zeng, Q. Tan, R. Liu, M. Zhong and Z. Zhong, *J. Magn. Magn. Mater.*, 2019, **473**, 155–160.
30 J. Jin, Y. Zhang, G. Bai, Z. Qian, C. Wu, T. Ma, B. Shen and M. Yan, *Sci. Rep.*, 2016, **6**, 30194.
31 A. K. Pathak, M. Khan, K. A. Gschneidner, R. W. McCallum, L. Zhou, K. Sun, M. J. Kramer and V. K. Pecharsky, *Acta Mater.*, 2016, **103**, 211–216.
32 X. Tang, H. Sepehri-Amin, M. Matsumoto, T. Ohkubo and K. Hono, *Acta Mater.*, 2019, **175**, 1–10.
33 Y. Wu, K. P. Skokov, L. Schäfer, F. Maccari, A. Aubert, H. Xu, H. Wu, C. Jiang and O. Gutfleisch, *Acta Mater.*, 2022, **235**, 118062.
34 G. Ding, S. Liao, J. Di, B. Zheng, S. Guo, R. Chen and A. Yan, *Acta Mater.*, 2020, **194**, 547–557.
35 X. Fan, K. Chen, S. Guo, R. Chen, D. Lee, A. Yan and C. You, *Appl. Phys. Lett.*, 2017, **110**, 172405.
36 X. Wu, J. Jin, Y. Tao, W. Chen, X. Peng and M. Yan, *J. Alloys Compd.*, 2021, **882**, 160731.
37 X. Fan, S. Guo, G. Ding, S. Fan, Z. Jin, R. Chen, S. Zhang and A. Yan, *J. Rare Earths*, 2022, **40**, 1480–1487.
38 B. Peng, T. Ma, Y. Zhang, J. Jin and M. Yan, *Scr. Mater.*, 2017, **131**, 11–14.
39 C. Abache and H. Oesterreicher, *J. Appl. Phys.*, 1986, **60**, 1114–1117.
40 X. G. Cui, X. H. Wang, G. C. Yin, C. Y. Cui, C. D. Xia, T. Y. Ma, C. Wang, B. X. Peng, J. X. Pan and P. Mei, *J. Alloys Compd.*, 2017, **726**, 846–851.
41 G. Huang, *Fenmo Yejin Cailiao Kexue yu Gongcheng/Materials Science and Engineering of Powder Metallurgy*, 2021, **26**, 40–46.
42 Z. Li, M. Yue, X. Liu, H. Zhang, W. Liu, Y. Li and Z. Zhang, *J. Magn. Magn. Mater.*, 2020, **505**, 166747.
43 Y. Harashima, K. Tamai, S. Doi, M. Matsumoto, H. Akai, N. Kawashima, M. Ito, N. Sakuma, A. Kato, T. Shoji and T. Miyake, *Phys. Rev. Mater.*, 2021, **5**, 013806.
44 T. Miyake, Y. Harashima, T. Fukazawa and H. Akai, *Sci. Technol. Adv. Mater.*, 2021, **22**, 543–556.
45 M. Gusenbauer, H. Oezelt, J. Fischbacher, A. Kovacs, P. Zhao, T. G. Woodcock and T. Schrefl, *npj Comput. Mater.*, 2020, **6**, 89.
46 L. Exl, J. Fischbacher, A. Kovacs, H. Özelt, M. Gusenbauer, K. Yokota, T. Shoji, G. Hrkac and T. Schrefl, *J. Phys.: Mater.*, 2019, **2**, 014001.
47 T. Lookman, P. V. Balachandran, D. Xue, J. Hogden and J. Theiler, *Curr. Opin. Solid State Mater. Sci.*, 2017, **21**, 121–128.
48 Q. Liang, A. E. Gongora, Z. Ren, A. Tiihonen, Z. Liu, S. Sun, J. R. Deneault, D. Bash, F. Mekki-Berrada, S. A. Khan, K. Hippalgaonkar, B. Maruyama, K. A. Brown, J. Fisher III and T. Buonassisi, *npj Comput. Mater.*, 2021, **7**, 188.
49 E. W. Huang, W.-J. Lee, S. S. Singh, P. Kumar, C.-Y. Lee, T.-N. Lam, H.-H. Chin, B.-H. Lin and P. K. Liaw, *Mater. Sci. Eng., R*, 2022, **147**, 100645.
50 B. Lei, T. Q. Kirk, A. Bhattacharya, D. Pati, X. Qian, R. Arroyave and B. K. Mallick, *npj Comput. Mater.*, 2021, **7**, 194.
51 R. Pollice, G. Dos Passos Gomes, M. Aldeghi, R. J. Hickman, M. Krenn, C. Lavigne, M. Lindner-D'Addario, A. Nigam, C. T. Ser, Z. Yao and A. Aspuru-Guzik, *Acc. Chem. Res.*, 2021, **54**, 849–860.
52 T. Lookman, P. V. Balachandran, D. Xue and R. Yuan, *npj Comput. Mater.*, 2019, **5**, 21.
53 Y. Zhang and C. Ling, *npj Comput. Mater.*, 2018, **4**, 25.
54 P. V. Balachandran, B. Kowalski, A. Sehirlioglu and T. Lookman, *Nat. Commun.*, 2018, **9**, 1668.
55 D. Xue, P. V. Balachandran, J. Hogden, J. Theiler, D. Xue and T. Lookman, *Nat. Commun.*, 2016, **7**, 11241.

56 J. Im, S. Lee, T.-W. Ko, H. W. Kim, Y. Hyon and H. Chang, *npj Comput. Mater.*, 2019, **5**, 37.
57 J. Li, Y. Zhang, X. Cao, Q. Zeng, Y. Zhuang, X. Qian and H. Chen, *Commun. Mater.*, 2020, **1**, 73.
58 Y. Chen, Y. Tian, Y. Zhou, D. Fang, X. Ding, J. Sun and D. Xue, *J. Alloys Compd.*, 2020, **844**, 156159.
59 L. Jiang, C. Wang, H. Fu, J. Shen, Z. Zhang and J. Xie, *J. Mater. Sci. Technol.*, 2022, **98**, 33–43.
60 H. Zhang, H. Fu, X. He, C. Wang, L. Jiang, L.-Q. Chen and J. Xie, *Acta Mater.*, 2020, **200**, 803–810.
61 D. Liu, K. Guo, F. Tang, F. Mao, X. Liu, C. Hou, H. Wang, H. Lu and X. Song, *Chem. Mater.*, 2019, **31**, 10117–10125.
62 Y. Iwasaki, R. Sawada, E. Saitoh and M. Ishida, *Commun. Mater.*, 2021, **2**, 31.
63 K. Guo, H. Lu, Z. Zhao, F. Tang, H. Wang and X. Song, *Comput. Mater. Sci.*, 2022, **205**, 111232.
64 X. Tang, J. Li, A. K. Srinithi, H. Sepehri-Amin, T. Ohkubo and K. Hono, *Scr. Mater.*, 2021, **200**, 113925.
65 Y. Zhang, T. C. Peck, G. K. Reddy, D. Banerjee, H. Jia, C. A. Roberts and C. Ling, *ACS Catal.*, 2022, **12**, 10562–10571.
66 Z. Li, L. E. K. Achenie and H. Xin, *ACS Catal.*, 2020, **10**, 4377–4384.
67 G. Lambard, T. T. Sasaki, K. Sodeyama, T. Ohkubo and K. Hono, *Scr. Mater.*, 2022, **209**, 114341.
68 X. B. Liu and Z. Altounian, *J. Appl. Phys.*, 2012, **111**, 07A701.
69 X. B. Liu, Z. Altounian, M. Huang, Q. Zhang and J. P. Liu, *J. Alloys Compd.*, 2013, **549**, 366–369.
70 *Scikit-learn*, **https://scikit-learn.org/stable/index.html**.
71 **https://www.webelements.com/**.
72 C. Wen, Y. Zhang, C. Wang, D. Xue, Y. Bai, S. Antonov, L. Dai, T. Lookman and Y. Su, *Acta Mater.*, 2019, **170**, 109–117.
73 R. J. Murdock, S. K. Kauwe, A. Y.-T. Wang and T. D. Sparks, *Integr. Mater. Manuf. Innov.*, 2020, **9**, 221–227.
74 D. Xue, D. Xue, R. Yuan, Y. Zhou, P. V. Balachandran, X. Ding, J. Sun and T. Lookman, *Acta Mater.*, 2017, **125**, 532–541.
75 R. Yuan, Y. Tian, D. Xue, D. Xue, Y. Zhou, X. Ding, J. Sun and T. Lookman, *Adv. Sci.*, 2019, **6**, 1901395.
76 R. Yuan, Z. Liu, P. V. Balachandran, D. Xue, Y. Zhou, X. Ding, J. Sun, D. Xue and T. Lookman, *Adv. Mater.*, 2018, **30**, 1702884.
77 X. Huang, C. Jin, C. Zhang, H. Zhang and H. Fu, *Mater. Des.*, 2021, **211**, 110177.
78 J. Li, H. Sepehri-Amin, T. Sasaki, T. Ohkubo and K. Hono, *Sci. Technol. Adv. Mater.*, 2021, **22**, 386–403.
79 X. Xia, M. Liu, T. Zhang, H. Wen, Q. Dong, L. Zhang, L. Zhou and M. Li, *Scr. Mater.*, 2020, **178**, 129–133.
80 F. Chen, L. Zhang, Y. Jin and Y. Cheng, *Mater. Charact.*, 2018, **144**, 547–553.
81 T. Zhang, S. Liu, Z. Wu, L. Zhang and R. Yu, *J. Alloys Compd.*, 2022, **903**, 163975.
82 J. S. Zhang, L. Z. Zhao, X. F. Liao, H. X. Zeng, D. R. Peng, H. Y. Yu, X. C. Zhong and Z. W. Liu, *Intermetallics*, 2019, **107**, 75–80.

 